Unconfined, melt edge electrospinning from multiple, spontaneous, self-organized polymer jets

2014 Mater. Res. Express 1 045304

(http://iopscience.iop.org/2053-1591/1/4/045304)

Materials Research
Express

Unconfined, melt edge electrospinning from multiple, spontaneous, self-organized polymer jets

Qingqing Wang[1], Colin K Curtis[2], Nagarajan Muthuraman Thoppey[3], Jason R Bochinski[2], Russell E Gorga[3] and Laura I Clarke[2]

[1] Jiangnan University, School of Textiles and Clothing, 1800 Lihu Avenue, Wuxi 214122, Jiangsu Province, People's Republic of China
[2] Department of Physics, NC State University, Raleigh, NC 27695-8202, USA
[3] Fiber and Polymer Science Program, NC State University, Raleigh, NC 27695-8301, USA
E-mail: liclarke@ncsu.edu and regorga@ncsu.edu

Received 28 August 2014, revised 27 October 2014
Accepted for publication 6 November 2014
Published 28 November 2014

Materials Research Express **1** (2014) 045304

doi:10.1088/2053-1591/1/4/045304

Abstract

Commercial grade polyethylene is melt electrospun from a thin film of unconfined molten polymer on a heated, electrically-grounded plate. Under the influence of an applied electric field, the melt spontaneously forms fingering perturbations at the plate edge which then evolve into emitting fiber-forming jets. Jet-to-jet spacing (~5 mm), which is dependent on the applied voltage amplitude, is in agreement with estimates from a simple theoretical treatment. The broad applicability of the approach is verified by spinning a second polymer —polycaprolactone. In both cases, the fabricated fibers are similar in quality to those obtained under needle melt electrospinning; however for this method, there are no nozzles to clog and an enhanced production rate up to 80 mg min^{-1} is achieved from approximately 20–25 simultaneous parallel jets. The process of jet formation, effective flow rates, cone-jet diameters, as well as limits on jet density and differences with polymer type are compared with theoretical models. This particular approach allows facile, high throughput micro- and nano-fiber formation from a wide variety of thermoplastics and other high viscosity fluids without the use of solvents or the persistent issues of clogging and pumping that hamper traditional methods, resulting in mechanically strong meso-scale fibers highly desirable for industrial applications.

Keywords: melt electrospinning, mesofibers, scale up, polyethylene, polycaprolactone

1. Introduction

Polymer nano- and microfibers are highly desirable as components in inexpensive porous materials having large surface-area-to-volume ratios for technological applications with significant societal impact, such as energy storage [1–4], air and water filtration [5–8], and biomedical uses [9, 10] including drug delivery [11–15], wound healing [16–18], and tissue scaffolding [19–24]. Single needle-based electrospinning is a widely-used approach to obtain high quality mesofibers from polymeric solutions [25, 26]. However, the production rate when electrospinning in this manner (0.01–0.1 $g\,h^{-1}$) is insufficient for viable industrial scale manufacturing. In addition, the resultant fibers fabricated may often be of poor mechanical quality, due in part to the need for choosing material systems having easy solubility, a criterion which cannot be met by many useful commercial thermoplastics. High entanglement and strong inter-chain interactions in such materials simultaneously result in both intrinsic strength and low solubility. Thermoplastics can be processed by needle-based electrospinning in the melt phase, however this approach is notoriously unpopular due to persistent fundamentally detrimental system issues such as needle clogging and relatively large fiber size (due in part to difficulties in pumping viscous fluids at very low feed rates) [27]. However, despite such challenges, recently research efforts in melt electrospinning have been rapidly increasing, driven by the potential of creating fibers having enhanced mechanical properties, the ability to utilize of a wider range of materials, and most importantly, increasing awareness of the environmental impact of manufacturing, which motivates interest in limiting or eliminating solvent use in industrial scale fabrication processes.

In this work, an unconfined spinning geometry, instead of a needle, is utilized where a strong electric field at the plate edge causes many parallel fiber-forming jets to spontaneously form on a sheet of molten polymer, and subsequently, electrospin a commercial polyethylene material creating meso-scale fibers. The broad applicability of this method is demonstrated by also melt spinning moderate molecular weight (<50 kDa) polycaprolactone. The obtained fiber quality is similar to that from a traditional melt needle set-up. Unconfined geometries [28–31] rely on electric-field induced spontaneous fluid perturbations to form jet sites, rather than mechanically pumping fluid through a confining nozzle. In such an open configuration, numerous simultaneous parallel jets produce the fibers, thus scaling the production rate by the increased jet number. This geometry is particularly well-suited for melt electrospinning as there are no nozzles to clog and fluid flow is determined by the interactions between fluid and field enabling dramatic tuning of effective feed rate. Thus, a wide-range of thermoplastic materials might be processed into meso- and nano-scale fibers utilizing this scheme. There is also interesting fundamental physics within such experiments: the process of spontaneous jet formation and the density of fiber-forming sites can be understood via fluid physics and conversely, serves as a tool to further understand the fundamental interactions between highly viscous, low ionic conductivity fluids and an applied electric field.

In this preliminary demonstration, continuous spinning with jet-to-jet spacing of ~5 mm is obtained and the resultant polyethylene fibers have diameters ranging from 3–30 μm. Although the size distribution is large, more than 50% of the fibers possess diameters <8 μm, representing a meso-scale size region that is difficult to access with conventional fiber-forming techniques. The polycaprolactone fibers produced by this method have a narrower diameter distribution centered around 2 μm. Melt electrospinning in needle geometries also commonly results in fiber diameters in the 1–10 μm range [27]: hence, there is no loss in fiber quality by utilizing the unconfined approach versus traditional needle electrospinning. The fiber forming jets are robust

(i.e., the jets are present indefinitely) and spontaneously re-form if inadvertently extinguished. Suitable operating temperatures, resultant melt viscosity, and appropriate voltage ranges for jet formation and maintenance were investigated.

In order to better elucidate the fundamental physics underlying fiber formation from high viscosity polymer melts in this geometry, the fluid mass flowing through each jet is measured (i.e., the flow rate), which is controlled by the fluid properties of the polymer melt and the applied electric field (determined by the system geometry and the applied external voltage). Distinct differences are observed when compared to the response of lower viscosity solutions in a similar set-up. The time scale over which the fluid spontaneously fingers and the experimentally observed jet density are both compared to theories where the interaction between fluid surface tension, viscosity, and the electric field determine the fluid response. Such an unconfined approach opens the possibility of higher throughput 'green' melt electrospinning of a variety of thermoplastic systems while retaining and potentially improving upon the fiber quality associated with the single-needle approach.

2. Experimental

2.1. Materials and characterization

ASPUN 6850A Fiber Grade Resin (Dow Chemical), a linear low density polyethylene (PE) with a manufacturer-stated melting temperature (T_m) of 131 °C, and polycaprolactone (Polysciences) (PCL) with a molecular weight range of 32–40 kDa and $T_m = \sim 60$ °C, were purchased and used without further purification. Polymer powder was obtained by successive cryo-grinding (SPEX CertiPrep 6750 freezer-mill) of either PE or PCL. Melt flow rate of the PE melts at different temperatures was measured with a melt flow rate meter (KTZ 400, Zhongshi Testing Equipment). The PE melt viscosity was measured with a capillary rheometer (Rosland RH10) over a temperature range of 160–280 °C and at a shear rate of 20 s^{-1}, which was the lowest rate at which data was highly reproducible. Dynamic scanning calorimetry (Perkin Elmer Diamond DSC-7, 25 °C to 145 °C at 10 °C min^{-1}) was utilized to confirm the PE T_m as within the range 131–135 °C, with no substantial change observed upon cryogrinding or after melt electrospinning at 200 °C for 60 min (with a 10–15 min of additional pre-heating, see below for details). Thermogravimetric analysis (Perkin Elmer Pyris) of PE at 280 °C for 1 h revealed 1.2% mass loss, indicating that the polymer is suitably stable for extended times at temperatures significantly above the working electrospinning temperatures.

2.2. Apparatus

The melt-electrospinning apparatus (figure 1) consists of an aluminum source plate ($14 \times 5 \times 0.5$ cm with additional upturned (0.8 cm tall) ends on three sides) placed directly on a commercial hot plate (Fisher Scientific model 11-500-78H). The 1 cm region of the source plate closest to the collector tapers in thickness to an edge value of 0.03 cm, which is ultimately where the spinning occurs. The source plate is placed off-center in order that the tapered edge protrudes over the hot plate edge by 1 cm. A type J thermocouple (Omega) is pressed between two ceramic ($1.5 \times 1.4 \times 0.5$ cm) plates (bound together by four screws) and affixed to the source plate to monitor temperature. The opposite side of the source plate is connected to ground potential with a thick wire. The 20×30 cm isolated aluminum collector (covered with

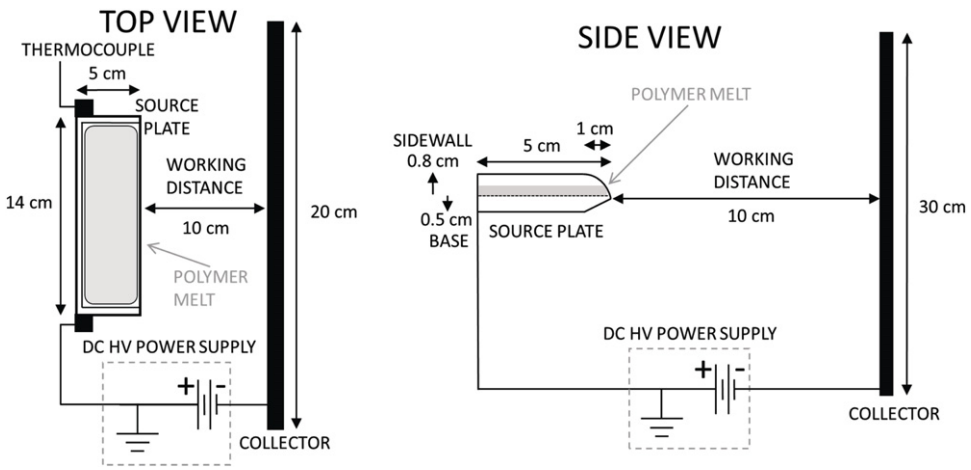

Figure 1. Schematic diagram of the experimental apparatus as viewed from above (top) and side. (Note: for clarity of viewing, hot plate not shown).

aluminum foil) situated 10 cm from the source plate is held at negative electric potential by a high voltage source (Glassman High Voltage Model FC60R2). The region between source and collector is only incidentally warmed via convection of ambient air from the source plate; it is not intentionally heated or temperature controlled. The spinning procedure was as follows: the hot plate is activated and allowed to reach the desired set temperature value. Once the set temperature is attained, 10 g of PE (or PCL) powder is distributed uniformly on the source plate. After the polymer material is fully melted (3–5 min) and the source plate has returned to the set temperature (an additional 10–15 min, as monitored via the thermocouple), the system is held at the set temperature for an additional 5 min before the negative polarity high voltage is applied to the collector, which subsequently initiates the fiber-forming, electrospinning process. PE fiber material fabrication rates are 1–2 grams per hour; thus the initial load of polymer mass on the plate is not significantly depleted during typical experiments of 60–90 min; PCL fabrication rates are $\sim 4.5\,\mathrm{g\,hr^{-1}}$.

2.3. Characterizing the electrospinning process

PE experiments were carried out under different temperature (140–200 °C) and high voltage (−41, −43, −45 kV applied to the collector) conditions. PCL experiments utilized 100 °C and −45 kV. A camcorder (Sony, Model DCR-SR68) viewed the source plate in order to characterize and temporally monitor the jet number and cone-jet morphology, as well as image the working region (between the source and collector) to visualize fiber formation. A Visual Instruments LED light (Model 900410) provided illumination of these regions. Still images were also taken with a Nikon 4500 SLR camera with 4× zoom. Reported data are averages of three separate experiments. Measurements of the cone-jet sizes are made from post-process analyzing the optical images utilizing Image-J software.

2.4. Fiber characterization

The mass throughput of the electrospun fibers per time was determined by weighing the aluminum foil on the collector. Fiber diameter, diameter distribution, and fiber morphology

were measured from scanning electron microscopy (SEM) images (Phenom FEI desktop SEM operating at 5 kV) where the fibrous mat samples were initially sputter-coated (Quoron Technologies, S67620) with Au-Pd at a thickness of ~10 nm to produce a conductive surface and reduce charging effects. Optical microscopy (Nikon Eclipse 50i POL Optical Microscope) images also confirmed the size results obtained from SEM. Image-J analysis utilized 100 individual measurements per image to determine the fiber diameter distribution.

2.5. Calculation of electric fields

Electric fields were simulated from the known experimental configuration and applied voltage amplitudes using Maxwell 3D, an ANSYS Corporation product. Pre-loaded regular rectangular shapes were used to represent the collector plate and surrounding air region. The geometry of the source plate was defined by using drawing tools followed by the unite objects operation. Optimized simulation parameters resulted in a minimum (maximum) mesh element dimension of <0.6 mm near the plate edge (149 mm in the homogenous air region) with a total of 943 519 mesh elements to provide sufficient spatial resolution in the experimentally important regions. Numerical values were computed for both the total capacitance of the system and electric field strength along a line between source and collector plates. A three-dimensional visual representation of electric field strength in the experimental region was generated.

3. Results and discussion

3.1. Spontaneous jet formation

The process of spontaneous jet formation from a polymer solution in an unconfined geometry (e.g., a thin film on a metal plate or a solution-filled thin edged bowl) has been discussed previously [28, 30, 31]. In the current system (figure 1), a strong electric field is formed at the sharp edge of the source plate, resulting in electric field strengths and gradients that are similar to those found in traditional single-needle electrospinning. In the simplest model, when high voltage is applied, the fluid develops a non-zero surface charge and appears to swell (e.g., elongates along the source-collector direction, pulling over the edge of the source plate), but surface tension prevents unconfined growth, instead forcing fingering as a compromise between the electrostatic and surface tension forces. Above a critical electric field value, such fingering perturbations are unstable and evolve into fluid expelling cone-jets [32–35]. The resultant structure consists of a relatively stable cone with mobile fluid moving through the jet (including the cone terminus) portion. Similar phenomena occur for melt electrospinning and the process is visualized in figure 2 for PE at a 180 °C plate temperature and −45 kV applied collector voltage: 3-4 min after application of high voltage several fluid perturbations form. The protrusions change shape and reorganize, new perturbations develop, and jetting (expulsion of fluid from the terminus of a perturbation) occurs after an additional 2–3 min (at 5.5 min in figure 2).

Over the next 15–20 min the number of fiber-forming jets continues to slowly grow (figure 3, at 170 °C and −45 kV). Once established, jets are robust—that is, they are present indefinitely. Note that the plate is oriented horizontally (figure 1) and the view in figure 2 is from above; gravity plays no role in the jet formation process.

The long time to form and organize instabilities is due to the high fluid viscosity of the polymer melt. A theoretical expression for the time for spontaneous fluid perturbation formation

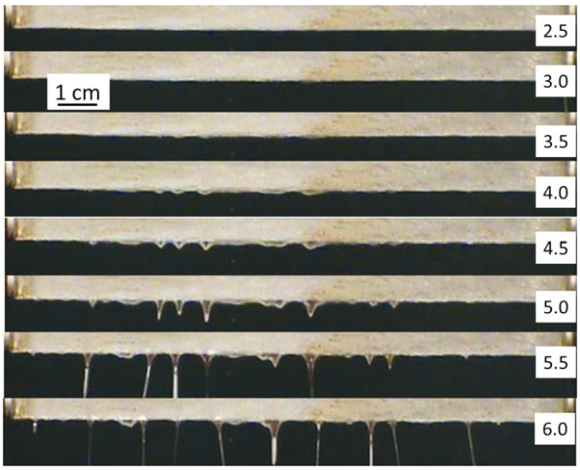

Figure 2. Sequential images of the polymer-melt coated plate edge showing the progression of the fluid with time (in minutes, right side) at 180 °C at an applied voltage of −45 kV. The plate is oriented horizontally and being viewed from above.

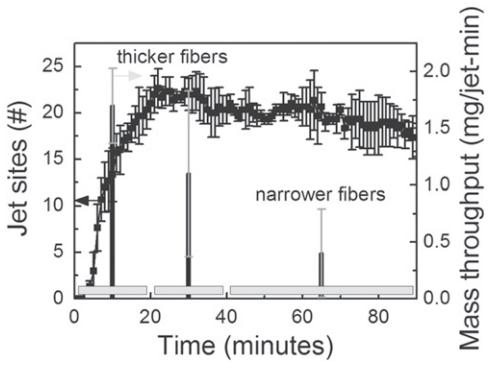

Figure 3. Jet number versus time for a 90 min experiment (left axis) with the source plate at 170 °C and −45 kV applied to the collector. The mass throughput per jet per minute over different time intervals is shown as gray rectangles (right axis). During the first 20 min the throughput per jet is high and fibers can be observed visually to be quite thick (~10 s of μm to 1 mm diameters). The throughput per jet has a lower value later in the process, and is associated with narrower fibers (~5 μm diameters). The total mass transferred from source plate to the collector over 90 min was 1.3 g, which is 13% of the total mass on the source (10 g).

from a planar sheet of highly viscous fluid under the influence of an electric field has been previously reported [36]:

$$\sigma = \frac{\gamma k^3 h^2}{2\eta}\left[\frac{\varepsilon_o E^2}{k\gamma} - 1\right], \tag{1}$$

where σ is the rate of formation (the inverse of the characteristic time, τ), γ is the surface tension, k is the characteristic wavenumber of the perturbations ($k = 2\pi/\lambda$), h is the film thickness (in our geometry, the coating of fluid on the edge of the plate between the source and collector), η is the viscosity, E is the electric field at the plate edge, and ε_o is the permittivity of free space.

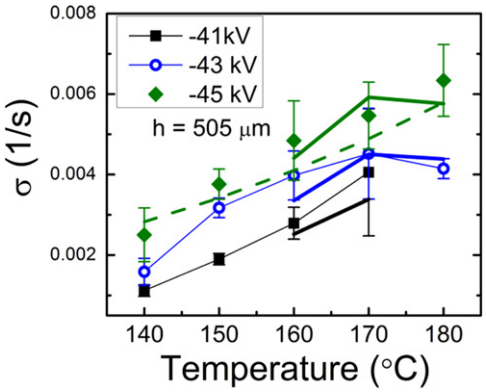

Figure 4. Inverse average time to spontaneous jet formation at the plate edge (σ) as a function of temperature for polyethylene. Points are data at −41 kV (black filled squares), −43 kV (blue open circles), or −45 kV (green filled diamonds). Thin solid lines are to guide the reader's eye; corresponding thick solid lines are fits using equation (2) over the temperature range where experimental viscosity measurements are available. Dotted line is fit (equation (2)) with extrapolated viscosity data over a wider temperature range.

This dispersion relation indicates that perturbation patterns with different characteristic wavelengths will grow at different rates. In other words, spontaneous fluctuations can occur with many different spatial patterns (wavelength or k values); those that will grow (rather than being damped out) will have a large σ value. Thus the k value at which σ is maximized will set the characteristic spacing for a particular system. The maximum occurs when $k = 2\varepsilon_o E^2/3\gamma$, or $\lambda = 2\pi(3\gamma/2\varepsilon_o E^2)$. This final characteristic spacing is independent of viscosity and film thickness (as discussed further in section 3.2). However, the rate at which the pattern forms depends on all variables and can be determined by substituting the dominant λ back into equation (1) to find:

$$\sigma = \frac{h^2}{2\eta}\left[\frac{4\varepsilon_o^3 E^6}{27\gamma^2}\right]. \tag{2}$$

Experimental measurements of σ were made at −45 kV (−41 and −43 kV) at 140–200 °C (140–180 °C) in 10 °C steps. The electric field can be estimated via simulation (see section 2.5 for details), and varies with distance from the plate edge at a given voltage. The value of $\gamma = 33.1\text{-}0.0390*\text{T}(^\circ\text{C})$ mN/m was obtained from reference [37]. Viscosity as a function of temperature was experimentally determined (see section 2.1 for details). Using h as a fitting parameter, the data and fit (from equation (2)) are presented in figure 4 with $h = 505\,\mu$m (thick solid lines). For self-consistency, the electric field value 500 μm from the plate edge (e.g., 2.3×10^6 V m^{-1} for −45 kV) is utilized in the fit. For the range where both experimental σ and viscosity values are available, the agreement between experiment and theory is good. The obtained value of h is reasonable given the images in figure 2 and the height of the film on the plate (perpendicular to the plate-collector direction) which is ∼1.6 mm (determined by the polymer mass, density, and the area of plate).

Examining the results from figure 4 in more detail shows that although both the surface tension and viscosity are temperature-dependent, the viscosity effect is much more dramatic and

dominates. In this regime at ~300 °C above the glass transition temperature ($T_g = -125$ °C), the temperature-dependence of the viscosity (η) is expected to follow an Arrhenius form $\eta = Ae^{E/kT}$ (where A is a constant, E is the activation energy, k is Boltzmann's constant, and T is the absolute temperature) with an activation energy of approximately 6 kcal mol^{-1} [38]. The experimental data was consistent with such a form with $E = 5.8$ kcal mol^{-1}, which was then used to estimate the viscosity at a wider range of temperatures (i.e., down to 140 °C). The σ values from the extrapolated viscosity are shown for the −45 kV case in figure 4 as a dotted line and correspond to the experimentally observed inverse jet initiation times.

This analysis indicates the process of fluid deformation, fingering, and ultimately jet formation in such an unconfined melt electrospinning process can be understood from fundamental fluid physics. In addition, after the jet formation and organization process, the characteristic spacing between fiber-forming fluid protrusions is also consistent with this fundamental model, as discussed in the next section.

3.2. Jet density

Equation (1) predicts a characteristic spacing between fluid perturbations as:

$$\lambda = 2\pi\left(3\gamma/2\varepsilon_o E^2\right) \tag{3}$$

which depends only on the applied electric field and surface tension, as this fundamental interaction causes the fingering to occur. In principle, each of these perturbations will transform into a fiber-forming jet site. For instance, the data in figure 3 gives an experimental value of 20 ± 3 active jets at −45 kV (180 °C) over the full 14 cm plate width or a characteristic $\lambda = 7.0 \pm 1.2$ mm, which is larger but consistent with the predicted value of 5.3 ± 0.8 mm. Figure 5 summarizes experimentally observed jet number versus the theoretical prediction (assuming a 10% error in both the computational predictions and temperature-dependent surface tension estimate) for an applied voltage of −45 kV. Generally the jet number is ~2/3 of the predicted value at temperatures of 160 to 190 °C and shows no particular dependence on temperature. The explanation for the slightly lower jet number is the presence of non-jetting perturbations, such as revealed in the characteristic image figure 5(c). The open regions indicated by arrows contain stable perturbations that have not developed into jets. Non-jetting perturbations are generally much wider than jets. In support of this hypothesis, figure 6 presents histograms of the jets spacing observed 1/2 h into the electrospinning process for plate temperatures of 170 °C, 180 °C and 190 °C (−45 kV applied). Although the presence of non-jetting perturbations results in a distribution of spacing, the most probable inter-jet distances are 5.0 ± 0.5 mm, 4.5 ± 0.5 mm, and 5.5 ± 0.5 mm, with increasing temperature, which are tightly clustered around the expected value for this temperature range, 5.2 ± 0.8 mm.

At a fixed temperature, as expected, decrease in voltage results in jet loss as the electric field is reduced (figure 5(b)), which decreases expected maximum jet density (equation (3)) and increases the characteristic time scale ($1/\sigma$, equation (2)).

At a constant applied voltage (−45 kV) and source plate temperatures of less than 160 °C, the jet number drops, with the jet density decreasing to half the higher temperature value by 140 °C. Based on the estimate utilized to fit figure 4, the viscosity increases from ~500 Pa-s at 170–180 °C to ~900 Pa-s at 140 °C. Significant decrease in jet number upon increasing viscosity has previously been observed in unconfined solution-phase electrospinning [28, 31] and attributed to several distinct causes at the lower viscosity levels (1–17 Pa-s) present in such

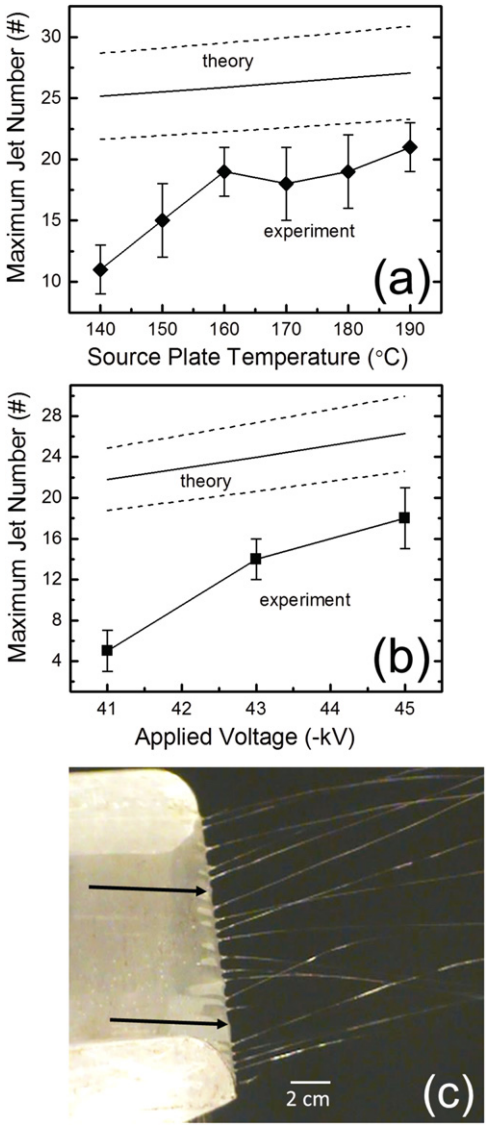

Figure 5. Observed maximum jet number for PE as a function of (a) source plate temperature (−45 kV) or (b) applied voltage at 170 °C. Theoretical predictions (straight line) are from equation (3) in text, with the dotted lines representing the range of uncertainty. (c) Image of electrospinning from a polymer melt coated source plate (PE at 170 °C, −45 kV) in steady state (i.e., after ∼30 min as shown in figure 3). The black arrows indicate non-jetting perturbations.

experiments. However, in the current experiments, these previously observed effects can be excluded. Prior theoretical and experimental work has established that both a minimum applied voltage/electric field and a minimum flow rate ($Q_{\min}$) are needed to initiate and maintain jetting [32, 33]. This constraint is particularly important in unconfined electrospinning where the flow rate is determined by the interaction between the fluid and the electric field, rather than mechanical or gravity-assisted metering such as in most confined electrospinning. However, as discussed in detail in section 3.3, the experimentally measured flow rate is stable ($0.06 \pm 0.007\ \mathrm{g\,h^{-1}}$/jet), even as the temperature drops from 190 °C to 140 °C at an applied

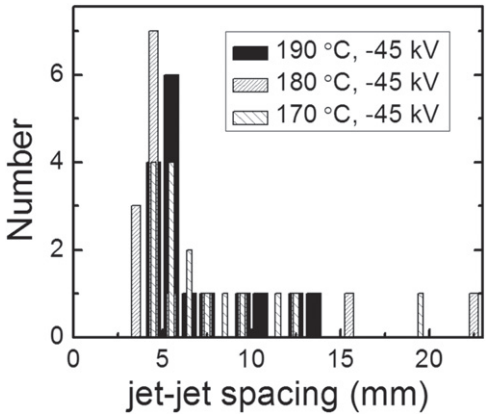

Figure 6. Histogram of observed inter-jet spacing at temperatures of 170, 180 and 190 °C (–45 kV applied). In all cases, the most probable value of jet-jet spacing is c.a. 5 mm, which matches with the theoretical prediction.

plate voltage of –45 kV. Alternatively, increased viscosity can increase cone-jet diameter, resulting in interactions between neighboring perturbations and ultimately setting new constraints on the maximum jet number [28]. Experimental measurement of the average cone-jet diameter confirms that is constant at 2.4 ± 0.2 mm (–45 kV, 140–190 °C). This observation also indicates that the average velocity within the jet, which is roughly $Q/\pi a^2$ (where a is the jet radius), does not change dramatically with temperature. Thus the loss of jets with decreasing temperature in the unconfined melt electrospinning approach does not appear to be related to flow.

The third possible cause of jet loss at high viscosity is more innate. As discussed in section 3.1, although the minimum spacing between cone-jets is largely dominated by interplay between the surface tension and the electric field (equation (3)), the rate at which the system samples this parameter space (including the presence of spontaneous perturbations that are then either enhanced or decay away at an exponential rate) is determined by the fluid viscosity. Fluid perturbation and ultimately jet formation depends on fluctuations at the source plate edge, which are damped by high viscosity. Taking the argument to the extreme limit, at some point, the material becomes solid at experimental time scales, and no perturbations will be present. Thus in the very viscous regime, the rate of perturbation formation decreases and the system is unable to reach the steady state value predicted by equation (3). This explanation is consistent with experimental observations at lower temperatures which show both fewer perturbations and a higher fraction of inactive (i.e., non-jetting) protrusions.

We conclude that the maximum jet density from a ASPUN 6850A melt is approximately 1.4 jets/cm (e.g., 20 persistent fiber-forming jets over the 14 cm length plate edge); this condition can be obtained over a range of temperatures (160–190 °C) at an applied voltage (–45 kV) which results in an electric field amplitude of $\sim 2.2 \times 10^6$ V m^{-1} at the plate edge. This electric field value is quite similar to (within 20%) that utilized previously for solution-phase electrospinning of polyethylene oxide (PEO, 400 kDa) in a similar plate configuration, where the solutions had a surface tension of ~60 mN m^{-1} (~2× that of ASPUN 6850A) [29–31]. (Note that the plate edge thickness in this work is larger (and thus associated with a lower electric field for a given voltage) than used previously [28].) In such a plate configuration, the maximum jet density obtained for 4 wt% and 6 wt% PEO solutions in water, was 0.9 jets/cm [28], limited by

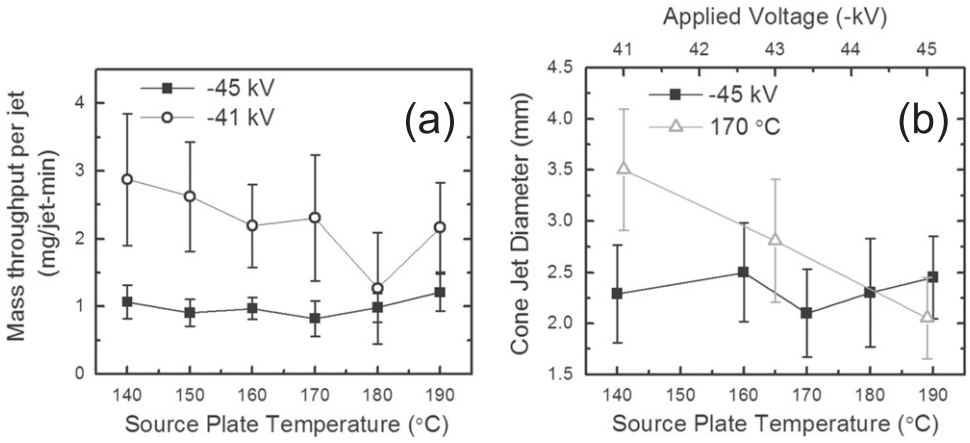

Figure 7. (a) Measured mass throughput per jet with an applied voltage of −41 kV (open circles) or −45 kV (filled squares) for varying source plate temperatures. (b) Measured cone-jet diameter from still images of the plate edge during electrospinning. Lower x axis: −45 kV for variable source plate temperatures (filled squares). Upper x axis: source plate fixed at 170 °C for differing applied voltages (open gray triangles).

jet-to-jet interactions. Thus, the results for melt jet density are very comparable to that previously obtained for electrospinning of solutions. As discussed in section 3.3, and as expected for a melt system, mass throughput per jet is significantly higher than when electrospinning from solution, where most of the volume passing through the jet is solvent and does not contribute to fiber mass and ultimately, the produced nanomaterial. This effect is one contribution that leads to melt electrospun fibers that are significantly thicker than their solution-phase equivalents (see section 3.4), and consistent with reported results for melt electrospinning using confined geometries.

3.3. Mass throughput per jet and fiber quality

Figure 7(a) summarizes measured average mass throughput per jet (averaged over a one hour experiment) as a function of source plate temperature for two applied voltages. These values are equivalent to volumetric flow rates in the range of 1–3 μL min^{-1}, which is comparable to rates utilized in single-needle melt electrospinning. For an applied voltage of −45 kV, the flow rate is constant with temperature. For an applied voltage of −41 kV, the flow rates are generally *higher* and exhibit a trend of decreasing flow rate with increasing temperature. In unconfined electrospinning, the flow rate is solely determined by the interactions between the electric field and the fluid, with a general approximate form of $Q = \pi a^2 v$ where both v (the velocity of the fluid in the jet) and a (the radius of the jet) depend on applied voltage and temperature which alter the viscosity η [28, 31, 39]. For instance, as also true for some forms of confined electrospinning [34], when electrospinning unconfined solutions, the most common effect of increased voltage is increased flow rate—that is the bigger driving force pulls more fluid from the surface, droplet, or orifice, increasing both the jet radius and the flow rate [28, 40]. Consequently, as experimentally verified in some confined cases [34], the velocity within the jet ($\sim Q/\pi a^2$) may actually decrease with increased applied voltage. Thus, fully understanding the electrospinning process requires measurement of *both* the flow rate *and* the cone-jet diameter. In unconfined electrospinning, experimentally measured cone-jet diameters reflect both the flow

rate and the local viscosity, which in viscous systems has been shown to determine the cone and jet radii [28]. In essence, at higher viscosity, it takes a longer distance to transition from a given maximum velocity at the center of the jet to zero velocity in the cone region. Figure 7(b) summarizes the experimentally measured cone-jet diameters at a constant applied voltage of −45 kV as a function of temperature (filled squares) and at a fixed source plate temperature of 170 °C as a function of voltage (open gray triangles). Cone-jets are measured within the first 30 min of active electrospinning.

The cone-jet diameters predictably follow the flow rate [41]. At an applied voltage of −45 kV, both the flow rate and cone-jet diameter are constant within error over the working temperature range. Thus, the system is quite robust in this range: altering the temperature affects the number of jets (as discussed in section 3.2) but functioning jets are not strongly impacted by the viscosity change as function of temperature. In contrast, jets formed at lower voltage are wider and have a larger flow rate.

Focusing on the effect of applied voltage, although actual flow rate and jet diameter are only rarely explicitly measured in confined melt electrospinning, the related quantity fiber diameter is reported. It is relatively common-place to observe an increase in fiber diameter with a decrease in applied electric field or voltage [42–49]. This trend is present for a wide-variety of polymers and for systems where the flow rate is explicitly controlled (by an independent pump) or conversely, controlled at least in part by the applied electric field. (For the highly viscous fluids and low flow rates required for melt electrospinning, explicit control of flow rate can be experimentally challenging.) In general the observation of smaller fiber diameter with increased applied voltage in confined melt electrospinning is attributed to an increase in the electric force on the melt (which provides enhanced stretching) [43, 45] or an increase in jet velocity [46]. This observation would indicate that in contrast to many solution-phase cases, increased electrical force (in this range) does not lead to increased flow rate. We make this assertion because in melt electrospinning, due to the absence of whipping region (in almost all cases) and lack of solvent evaporation, flow rate is strongly correlated to fiber diameter [42, 44]. Although experimental constraints generally restrict the possible applied voltage amplitude to a narrow range, when a larger voltage range is tested, some workers see a flattening of response or a slight increase in fiber diameter at the highest voltage (i.e., applied electric field) [44, 46, 48] which indicates that at sufficiently high electric fields the flow rate may increase, a response more similar to that seen in solution-phase electrospinning.

In the unconfined case, the results in figure 7 clearly show that the flow rate (and the associated cone-jet diameter) increases with decreased applied voltage amplitude. These observations indicate a shear thinning effect: the larger the electrostatic force applied to the melt, the lower the viscosity. Thus, as the voltage level is decreased, the effective viscosity increases, leading to a wider cone-jet and a higher flow rate. In this hypothesis, the fluid velocity is lower at the lower applied voltages: the increase in flow rate is due to the increase in jet diameter due to the viscosity increase at lower shear rates. Hence, the very different viscoelastic properties of the melt result in a different response to the voltage than observed in solution-phase electrospinning. Furthermore, in the unconfined melt case, any direct increase in 'stretching force' on the fiber beyond the jet due the increased applied voltage is likely hidden by flow rate effects.

The single-needle electrospinning experiments in literature reported different fiber diameter dependence in different voltage ranges, which may be strongly influenced by effective flow rate. Here we observe a combined dependence of flow rate on both voltage and

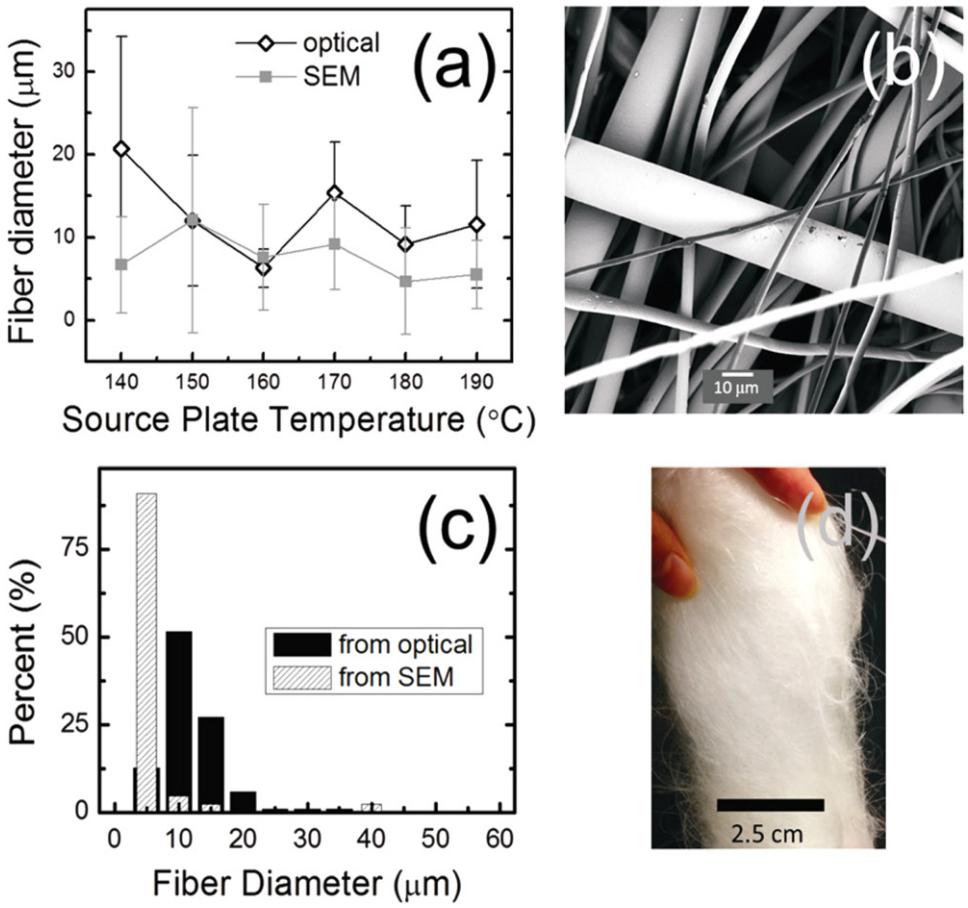

Figure 8. (a) Fiber diameter as a function of plate temperature at −45 kV applied voltage as determined from analysis of scanning electron microscopy (SEM) (filled gray squares) or optical images (open diamonds). Error bars are one standard deviation. (b) SEM Image of melt electrospun fibers from the source plate at 160 °C and −45 kV applied voltage. (c) Histogram of fiber diameter distribution for 180 °C (−45 kV) showing distribution from both SEM and optical image analysis. (d) A collection of melt electrospun PE fibers fabricated after ∼60 min of electrospinning.

temperature. For example (figure 7(a)), when the applied voltage is small (−41 kV) then as the temperature increases, a decreased viscosity results in a decreased flow rate, which is consistent with a smaller jet diameter. However, one could easily imagine an alternative response when viscosity is lowered, such as that seen in unconfined electrospinning of polymer solutions, which would result in an increase in flow rate: decreased viscosity leads to a higher jet velocity and thus a wider jet. At the lower viscosities accessed with −45 kV applied, the flow rate (and cone-jet diameter) is now stable with temperature, which is likely the effect to these two counteracting trends. Here, the increase in jet velocity cancels the jet narrowing and the flow rate is stable with temperature.

Characteristic images of the resultant PE fibers and fiber diameter analysis are shown in figure 8. The diameter of fibers formed with −45 kV applied (averaging over the entire collection time), shows little dependence on source plate temperature as might be expected due to the constant flow rate. Here, both optical and scanning microscopy images have been utilized

to determine fiber diameter. Optical images ensure sampling of wider fibers and analysis of a large number of fibers, however the depth of field samples both in-focus and out-of-focus (i.e., slightly apparently broadened) objects. Thus, the average fiber diameter determined from electron microscopy (SEM) is consistently smaller but the values from the two techniques overlap within error. Overall, at all working temperatures from 140–190 °C, fibers with an average diameter of 10 μm are formed, with a large distribution of fiber sizes. These results are similar to the fiber quality produced in many confined melt electrospinning schemes and confirm that the general unconfined melt electrospinning process is efficient and stable over a relatively wide temperature range. Figure 8(d) shows an example of the mass of fibers formed over an hour of electrospinning: fibers are tangled but separate and can be easily removed from the collector.

Visual observations of the electrospinning process reveal that the initial fibers formed upon jetting are very thick and that jet diameters narrow with time, leading to correspondingly thinner fibers. This observation is supported by measurement of flow rate as a function of time (figure 3), determined by measuring mass throughput in repeated experiments of different time duration. The flow rate drops from 1.7 mg per jet-minute during the first 20 min of operation where the jet number is still slowly increasing to 0.4 mg per jet-minute for electrospinning time intervals greater than 40 min. Thus, one reason for the large distribution of fiber diameters is the change in flow rate which occurs as a function of spinning time. The long equilibrium time of the system may be related to flow induced changes in viscosity and although small, change in the film thickness on the plate may lead to both a slight decrease in jet number and reduced flow rate. Nevertheless, these results indicate that under suitable conditions fibers as fine as ~5 μm diameter can be fabricated from an unconfined melt electrospinning at a fabrication rate of ~0.5 g h^{-1}.

3.4. Unconfined melt electrospinning of polycaprolactone

To illustrate the generality of this approach, a moderate molecular weight polycaprolactone (PCL) (43–50 kD, T_m = 58–60 °C) was also melt electrospun. Figure 9 summarizes the results of PCL electrospinning with a plate temperature of 100 °C and an applied voltage of −45 kV. Using an estimated surface tension of 37.3 mN m^{-1} at 100 °C [50], the same electric field value as utilized in section 3.2, and equation (3), the predicted jet number is estimated as 18.6 ± 4.2, which matches well with the observed experimental value (achieved from 40–90 min in figure 9) of 19.9 ± 0.8. Electrospinning from an average of 18.5 ± 3.5 jets over the entire 90 min produced 7.1 ± 1.0 g of microfibers, resulting in an average flow rate per jet of 4.2 ± 1.0 mg min^{-1}. This value is higher than that observed for ASPUN polyethylene (ranging from 0.3–1.7 mg min^{-1}). Despite the higher flow rate, cone-jet diameter was consistently smaller (1.8 ± 0.3 mm) than for ASPUN, which indicates a lower viscosity for the PCL melt. Lower viscosity is consistent with observations of jet formation, which occurs more rapidly with the first expelling jets forming within 3–4 min after application of voltage, and with the fabrication of thinner fibers with an average diameter of 1.8 ± 1.2 μm (from SEM image analysis). Such fiber diameters are fully consistent with those commonly obtained from needle-based melt electrospinning of similar material; however at a much higher production rate where spinning can be maintained for many hours without needle clogging.

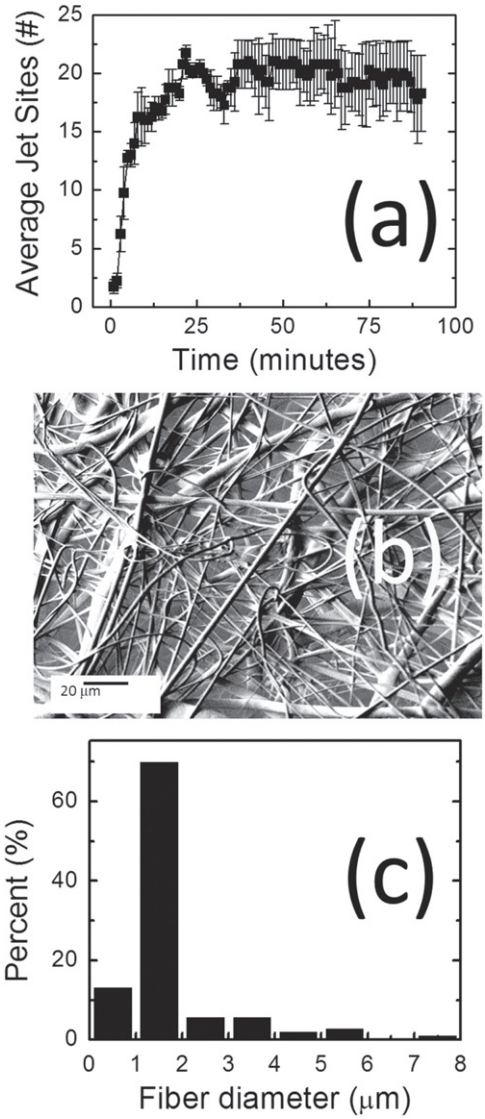

Figure 9. (a) Average jet number as a function of time for PCL melt electrospinning at 100 °C and −45 kV. (b) SEM Image of the resulting melt electrospun fibers. (c) Figure diameter distribution with an average value of $1.8 \pm 1.2\,\mu$m.

4. Conclusions

Unconfined melt electrospinning is demonstrated with two different polymer systems. Jet-to-jet spacing of ∼5 mm is obtained in both cases, which is generally much smaller than the possible site spacing when electrospinning from multiple confined sources, e.g., an array of needles. Fundamental analysis shows the important physical parameters that control inter-jet spacing and flow rate. As in confined melt electrospinning, one of the most dominant effects influencing the process is the melt viscosity. Comparing results from PE at 170–190 °C (40–60 °C above T_m) and PCL at 100 °C (40 °C above T_m), which have similar surface tension values (∼37 mN m^{-1} and 26 mN m^{-1}, respectively), we observe that for the lower viscosity material system (PCL) produces the expected jet number and provides high throughput per jet with a lower resultant

fiber diameter. For the higher viscosity polymer system (PE), the time to form or re-form perturbations and jets is longer, not all perturbations transition into fiber-forming jets, and the formed fibers have a larger diameter. However, electrospinning, with moderate quality fibers and significant throughput, is still readily achievable. The effect of shear thinning on flow rate is clearly demonstrated for PE, indicating that the strongest result of increased voltage is a decrease in effective viscosity: utilizing such an approach may be useful in spinning high quality fibers from innately high-viscosity melt systems. From a technological perspective, the fabrication of fibers of the same quality as in the needle approach but at a much higher throughput (up to $80\,\mathrm{mg\,min^{-1}}$) with no possibility of nozzle clogging opens the door to significant-scale production of microstructures (and perhaps even nanostructures) from a wide variety of thermoplastic systems, even high viscosity melts which may not be suitable for needle electrospinning. From a fundamental perspective, these experiments increase our understanding of highly viscous fluids under the influence of a strong electric field.

Acknowledgements

This work was supported by NSF CMMI-0800237 and the Faculty Research and Professional Development Fund at NC State University. The authors thank Ms Judy Elson for assistance with SEM measurements, Ya Ting Su for performing melt rheology, Mr Hai Bui and Mr Dzung Nguyen for technical assistance, and Dr Behman Pourdeyhimi for his kind donation of the PE material. QW acknowledges support from the State Scholarship Fund from the China Scholarship Council.

References

[1] Cavaliere S, Subianto S, Savych I, Jones D J and Roziere J 2011 Electrospinning: designed architectures for energy conversion and storage devices *Energy Environ. Sci.* **4** 4761–85

[2] Long Y Z, Yu M, Sun B, Gu C Z and Fan Z Y 2012 Recent advances in large-scale assembly of semiconducting inorganic nanowires and nanofibers for electronics, sensors and photovoltaics *Chem. Soc. Rev.* **41** 4560–80

[3] Mao X W, Hatton T A and Rutledge G C 2013 A Review of electrospun carbon fibers as electrode materials for energy storage *Curr. Org. Chem.* **17** 1390–401

[4] Ramakrishna S, Fujihara K, Teo W E, Yong T, Ma Z W and Ramaseshan R 2006 Electrospun nanofibers: solving global issues *Mater. Today* **9** 40–50

[5] Botes M and Cloete T E 2010 The potential of nanofibers and nanobiocides in water purification *Crit. Rev. Microbiol.* **36** 68–81

[6] Thavasi V, Singh G and Ramakrishna S 2008 Electrospun nanofibers in energy and environmental applications *Energy Environ. Sci.* **1** 205–21

[7] Feng C, Khulbe K C, Matsuura T, Tabe S and Ismail A F 2013 Preparation and characterization of electrospun nanofiber membranes and their possible applications in water treatment *Separ. Purif. Technol.* **102** 118–35

[8] Kaur S, Sundarrajan S, Rana D, Sridhar R, Gopal R, Matsuura T and Ramakrishna S 2014 Review: the characterization of electrospun nanofibrous liquid filtration membranes *J. Mater. Sci.* **49** 6143–59

[9] Goh Y F, Shakir I and Hussain R 2013 Electrospun fibers for tissue engineering, drug delivery, and wound dressing *J. Mater. Sci.* **48** 3027–54

[10] Dasdemir M, Topalbekiroglu M and Demir A 2013 Electrospinning of thermoplastic polyurethane microfibers and nanofibers from polymer solution and melt *J. Appl. Polym. Sci.* **127** 1901–8

[11] Liang D, Hsiao B S and Chu B 2007 Functional electrospun nanofibrous scaffolds for biomedical applications *Adv. Drug Deliv. Rev.* **59** 1392–412
[12] Sill T J and von Recum H A 2008 Electro spinning: applications in drug delivery and tissue engineering *Biomaterials* **29** 1989–2006
[13] Yoo H S, Kim T G and Park T G 2009 Surface-functionalized electrospun nanofibers for tissue engineering and drug delivery *Adv. Drug Deliv. Rev.* **61** 1033–42
[14] Coneski P N, Nash J A and Schoenfisch M H 2011 Nitric oxide-releasing electrospun polymer microfibers *ACS Appl. Mater. Interfaces* **3** 426–32
[15] Lavin D M, Stefani R M, Zhang L, Furtado S, Hopkins R A and Mathiowitz E 2012 Multifunctional polymeric microfibers with prolonged drug delivery and structural support capabilities *Acta Biomater.* **8** 1891–900
[16] Jayakumar R, Prabaharan M, Nair S V and Tamura H 2010 Novel chitin and chitosan nanofibers in biomedical applications *Biotechnol. Adv.* **28** 142–50
[17] Rieger K A, Birch N P and Schiffman J D 2013 Designing electrospun nanofiber mats to promote wound healing—a review *J. Mater. Chem.* B **1** 4531–41
[18] Sell S, Barnes C, Smith M, McClure M, Madurantakam P, Grant J, McManus M and Bowlin G 2007 Extracellular matrix regenerated: tissue engineering via electrospun biomimetic nanofibers *Polym. Int.* **56** 1349–60
[19] Jang J H, Castano O and Kim H W 2009 Electrospun materials as potential platforms for bone tissue engineering *Adv. Drug Deliv. Rev.* **61** 1065–83
[20] Martins A, Reis R L and Neves N M 2008 Electrospinning: processing technique for tissue engineering scaffolding *Int. Mater. Rev.* **53** 257–74
[21] Subramanian A, Krishnan U M and Sethuraman S 2009 Development of biomaterial scaffold for nerve tissue engineering: biomaterial mediated neural regeneration *J. Biomed. Sci.* **16** 108
[22] McCullen S D, Ramaswamy S, Clarke L I and Gorga R E 2009 Nanofibrous composites for tissue engineering applications *Wiley Interdiscip. Rev.-Nanomed. Nanobiotechnol.* **1** 369–90
[23] Kwon I K, Kidoaki S and Matsuda T 2005 Electrospun nano- to microfiber fabrics made of biodegradable copolyesters: structural characteristics, mechanical properties and cell adhesion potential *Biomaterials* **26** 3929–39
[24] Surrao D C, Hayami J W S, Waldman S D and Amsden B G 2010 Self-crimping, biodegradable, electrospun polymer microfibers *Biomacromolecules* **11** 3624–9
[25] Luo C J, Stoyanov S D, Stride E, Pelan E and Edirisinghe M 2012 Electrospinning versus fibre production methods: from specifics to technological convergence *Chem. Soc. Rev.* **41** 4708–35
[26] Greiner A and Wendorff J H 2007 Electrospinning: a fascinating method for the preparation of ultrathin fibres *Angew. Chem.-Int. Ed.* **46** 5670–703
[27] Hutmacher D W and Dalton P D 2011 Melt electrospinning *Chem.-Asian J.* **6** 44–56
[28] Roman M P, Thoppey N M, Gorga R E, Bochinski J R and Clarke L I 2013 Maximizing spontaneous jet density and nanofiber quality in unconfined electrospinning: the role of interjet interactions *Macromolecules* **46** 7352–62
[29] Thoppey N M, Bochinski J R, Clarke L I and Gorga R E 2010 Unconfined fluid electrospun into high quality nanofibers from a plate edge *Polymer* **51** 4928–36
[30] Thoppey N M, Bochinski J R, Clarke L I and Gorga R E 2011 Edge electrospinning for high throughput production of quality nanofibers *Nanotechnology* **22** 345301
[31] Thoppey N M, Gorga R E, Bochinski J R and Clarke L I 2012 Effect of solution parameters on spontaneous jet formation and throughput in edge electrospinning from a fluid-filled bowl *Macromolecules* **45** 6527–37
[32] Higuera F J 2010 Electrodispersion of a liquid of finite electrical conductivity in an immiscible dielectric liquid *Phys. Fluids* **22** 112107
[33] Higuera F J 2010 Numerical computation of the domain of operation of an electrospray of a very viscous liquid *J. Fluid Mech.* **648** 35–52

[34] Reneker D H, Yarin A L, Zussman E and Xu H 2007 *Advances in Applied Mechanics* ed H Aref and E Van Der Giessen vol 41 (San Diego, CA: Elsevier) pp 43–195
[35] Reznik S N, Yarin A L, Theron A and Zussman E 2004 Transient and steady shapes of droplets attached to a surface in a strong electric field *J. Fluid Mech.* **516** 349–77
[36] Miloh T, Spivak B and Yarin A L 2009 Needleless electrospinning: Electrically driven instability and multiple jetting from the free surface of a spherical liquid layer *J. Appl. Phys.* **106** 114910
[37] Potschke P, Pionteck E and Stutz H 2002 Surface tension, interfacial tension, and morphology in blends of thermoplastic polyurethanes and polyolefins: I. Surface tension of melts of TPU model substances and polyolefins *Polymer* **43** 6965–72
[38] Wang J and Porter R S 1995 On the viscosity-temperature behavior of polymer melts *Rheol. Acta* **34** 496–503
[39] de Gennes P-G, Brochard-Wyart F and Quere D 2010 *Capillarity and Wetting Phenomena* (New York: Springer)
[40] Higuera F J 2008 Breakup of a supported drop of a viscous conducting liquid in a uniform electric field *Phys. Rev.* E **78** 016314
[41] Ganan-Calvo A M 1997 On the theory of electrohydrodynamically driven capillary jets *J. Fluid Mech.* **335** 165–88
[42] Zhmayev E, Zhou H and Joo Y L 2008 Modeling of non-isothermal polymer jets in melt electrospinning *J. Non-Newton. Fluid Mech.* **153** 95–108
[43] Mota C, Puppi D, Gazzarri M, Bartolo P and Chiellini F 2013 Melt electrospinning writing of three-dimensional star poly(E-caprolactone) scaffolds *Polym. Int.* **62** 893–900
[44] Detta N, Brown T D, Edin F K, Albrecht K, Chiellini F, Chiellini E, Dalton P D and Hutmacher D W 2010 Melt electrospinning of polycaprolactone and its blends with poly(ethylene glycol) *Polym. Int.* **59** 1558–62
[45] Lyons J, Li C and Ko F 2004 Melt-electrospinning: I. Processing parameters and geometric properties *Polymer* **45** 7597–603
[46] Deng R J, Liu Y, Ding Y M, Xie P C, Luo L and Yang W M 2009 Melt electrospinning of low-density polyethylene having a low-melt flow index *J. Appl. Polym. Sci.* **114** 166–75
[47] Zhou H J, Green T B and Joo Y L 2006 The thermal effects on electrospinning of polylactic acid melts *Polymer* **47** 7497–505
[48] Hao M F, Liu Y, He X T, Ding Y M and Yang W M 2011 *Advanced Polymer Science and Engineering* ed C H Wang *et al* (Stafa-Zurich: Trans Tech) pp 129–34
[49] Wang X N, Xu Y, Wei Q F and Cai Y B 2011 *Advanced Textile Materials, Pts 1-3* ed X M Qian and H W Liu (Stafa-Zurich: Trans Tech) pp 1550–6
[50] Sauer B B and Dee GT 2002 Surface tension and melt cohesive energy density of polymer melts including high melting and high glass transition polymers *Macromolecules* **35** 7024–30